Long-range ballistic propagation of carriers in methylammonium lead iodide perovskite thin films

Jooyoung Sung [1,2], Christoph Schnedermann [1,2], Limeng Ni [1], Aditya Sadhanala[1,3],
Richard Y. S. Chen[1], Changsoon Cho[1,4,6], Lee Priest[2], Jong Min Lim [2,7], Hyun-Kyung Kim [5,8],
Bartomeu Monserrat[1], Philipp Kukura [2]* and Akshay Rao [1]*

The performance of semiconductor devices is fundamentally governed by charge-carrier dynamics within the active materials[1-6]. Although advances have been made towards understanding these dynamics under steady-state conditions, the importance of non-equilibrium phenomena and their effect on device performances remains elusive[7,8]. In fact, the ballistic propagation of carriers is generally considered to not contribute to the mechanism of photovoltaics (PVs) and light-emitting diodes, as scattering rapidly disrupts such processes after carrier generation via photon absorption or electric injection[9]. Here we characterize the spatiotemporal dynamics of carriers immediately after photon absorption in methylammonium lead iodide perovskite films using femtosecond transient absorption microscopy (fs-TAM) with a 10 fs temporal resolution and 10 nm spatial precision. We found that non-equilibrium carriers propagate ballistically over 150 nm within 20 fs of photon absorption. Our results suggest that in a typical perovskite PV device operating under standard conditions, a large fraction of carriers can reach the charge collection layers ballistically. The ballistic transport distance appears to be limited by energetic disorder within the materials, probably due to disorder-induced scattering. This provides a direct route towards optimization of the ballistic transport distance via improvements in materials and by minimizing the energetic disorder. Our observations reveal an unexplored regime of carrier transport in perovskites, which could have important consequences for device performance.

Organic–inorganic metal halide perovskites have attracted much attention in recent years due to their remarkable semiconductor properties[10-12]. Despite being solution processed, these materials appear to be largely defect tolerant, which results in long carrier lifetimes and high photoluminescence (PL) quantum yields, facilitating an excellent device performance[1-6,13]. The associated charge-carrier transport has been probed under steady-state or quasi-steady-state conditions via indirect means, such as PL quenching, which indicate carrier diffusion lengths in excess of 1 μm in methylammonium lead triiodide (MAPbI$_3$), the prototypical organic–inorganic metal

halide perovskite system[14,15]. Previous time-resolved microscopy studies resolved the diffusive motion of carriers on picosecond timescales, but were insensitive to the ultrafast spatial dynamics of non-equilibrium carriers[16,17] due to a limited temporal resolution and spatial precision (300 fs and 50 nm).

To provide experimental access to the largely unexplored regime of spatiotemporal dynamics that occurs on the ultrafast timescales usually associated with quantum coherent phenomena[18], we combined the extreme temporal resolution provided by ultrafast spectroscopy with the nanometre-level localization capabilities of high-performance optical microscopes[19]. Delivering a simultaneously near diffraction-limited (264 nm full-width half-maximum (FWHM), which is equivalent to a width (σ) of 112 nm) and transform-limited (9.2 fs) pump pulse centred at 580 nm to the sample allows for tight spatiotemporal control of photon absorption (Fig. 1a and Supplementary Sections 1 and 2)[20]. Probing the ensuing carrier dynamics with a counterpropagating and loosely focused (15 μm FWHM and σ of 6.4 μm) transform-limited (6.8 fs) probe pulse in the near infrared, enabled us to simultaneously monitor the spatiotemporal and spectral dynamics after the initial photoexcitation. We followed the evolution of the photoinduced dynamics by comparing the spatial distribution of the carrier population as a function of time, which enabled us to quantify the carrier motion with spatial precision far below the diffraction limit (10 nm), limited only by the signal-to-noise characteristics of the system (Supplementary Sections 3 and 4)[17,21]. Unlike X-ray or electron-based probes, visible light pulses are highly sensitive to a range of electronic dynamics in semiconductor materials. Moreover, by achieving sub-10 fs pulse durations for both pump and probe pulses, we accessed the spatially evolving carrier dynamics of both non- and quasi-equilibrium states[22].

We focused our investigation on the spatial carrier dynamics of the extremely well-characterized methylammonium lead iodide system (MAPI$_{3-x}$Cl$_x$) (refs. [15,23,24]). To probe the effect of the underlying film morphology on carrier transport at early times, thin films with varying morphology were prepared. These are labelled films 1, 2 and 3. Film 1 was prepared using a single-step cold-casting method.
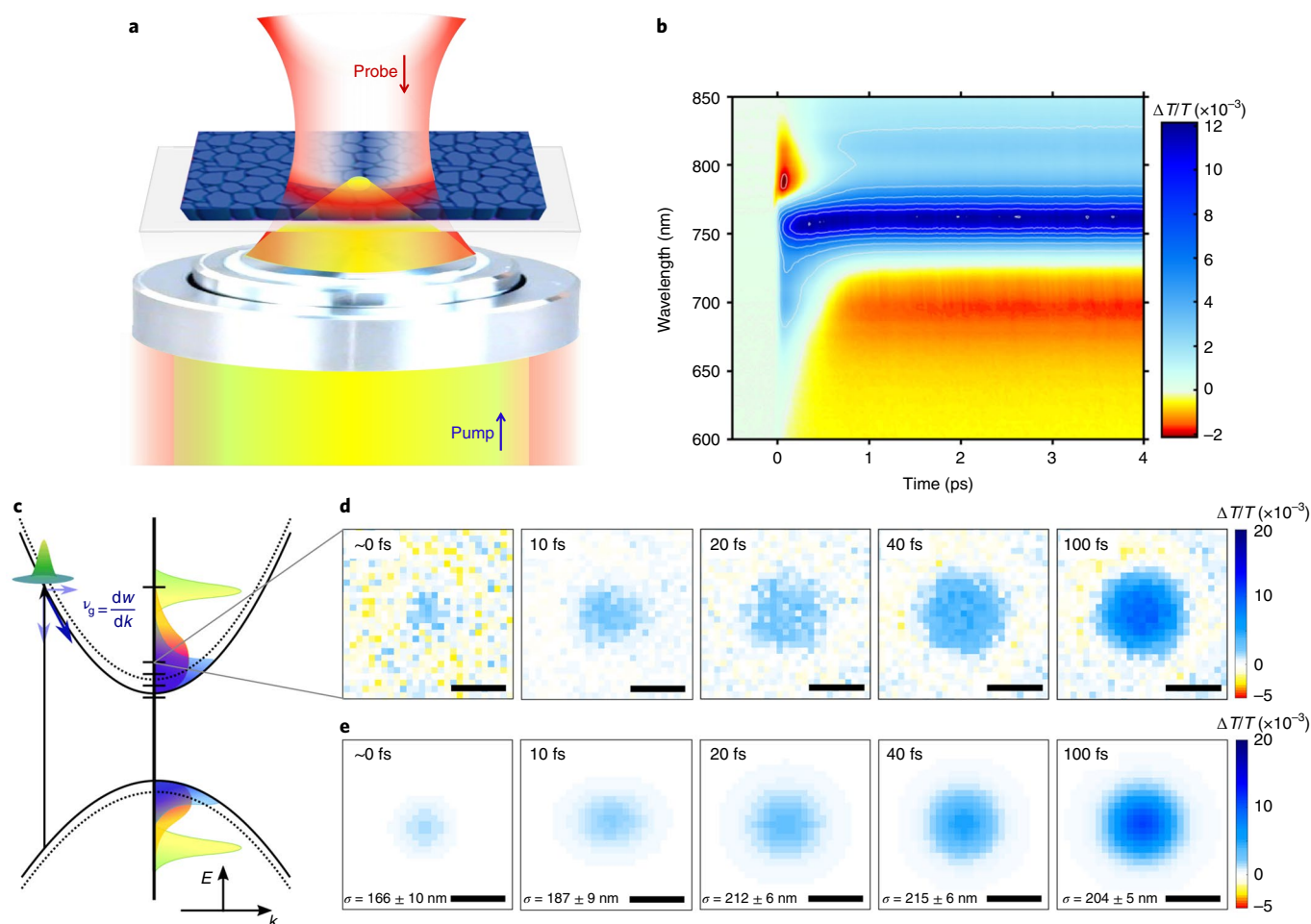
Fig. 1 | Representative transient absorption spectroscopy and microscopy results of MAPI$_{3-x}$Cl$_x$ thin film. a, Schematic of fs-TAM. A near diffraction-limited (σ of 112 nm) and transform-limited (9.2 fs, 580 nm) pump pulse was delivered to the sample with a counterpropagating and loosely focused (σ of 6.4 μm) <6.8 fs probe pulse. Comparison of the snapshots of the spatial distribution of the carrier population enabled us to measure carrier motion with spatial precision (10 nm) far below the diffraction limit, limited only by the signal-to-noise ratio of the system. **b**, Transient differential transmission map at an initial carrier density of 1.28×10^{17} cm^{-3}. **c**, Schematic diagram of carrier dynamics at early times: the initial photon absorption leads to the formation of a non-equilibrium carrier population at the pump energy (green-to-yellow shaded region). The excited charge carriers induce the shrinkage of the original band gap (dashed lines), referred to as band-gap renormalization (solid lines). Carrier–carrier scattering then leads to thermalization and the formation of a quasi-equilibrium 'hot-carrier' population on sub-100 fs timescales (yellow-to-red shaded region) and the hot carriers then cool to the lattice temperature (blue-to-purple shaded region). At the earliest times carriers can propagate as wavepackets (green shaded wavepacket) at the group velocity (v_g, where k is the wavevector, w is the wave's angular frequency and E is energy). **d**, Representative fs-TAM images at 720 nm (1.72 eV) recorded as a function of pump–probe delay. A spectral bandwidth of 10 nm was achieved by inserting adequate bandpass filters in the imaging path. The signal intensities of fs-TAM images at a 0 fs and a 10 fs pump–probe delay are scaled by factors of 5 and 2, respectively, for clarity. **e**, The corresponding carrier distribution functions fitted with isotropic 2D Gaussian functions. The σ values represent the extracted width of the carrier distribution at each pump–probe delay. Scale bars, 500 nm.

Film 2 was prepared using a single-step hot-casting method[25] and film 3 was fabricated in air using a single-step cold-casting method to fabricate a disordered film. Full details of the sample preparation are given in Methods (Supplementary Fig. 1). The ground-state absorption spectrum of all the films exhibits a peak in the wavelength range from 700 to 760 nm, which corresponds to the band-gap energy (E_g) of the films (Supplementary Fig. 2)[7]. The early-time dynamics of the films as investigated by conventional transient absorption spectroscopy (Fig. 1b and Supplementary Figs. 3 and 4) are consistent with those in previous reports[26–28]. The details of the involved transient species are discussed in Supplementary Section 5. We emphasize two specific observations that are important for the analysis of the time-resolved microscope results: first, a strong photobleaching band dominates the transient absorption signal between 750 and 760 nm with a broad high-energy tail in the 600–750 nm

range, which is mainly attributed to the phase-space filling effect[29]. Second, early time relaxation dynamics of carriers, such as thermalization and cooling, which generally occur in less than a picosecond, depend strongly on the carrier density. As the carrier density increases, thermalization accelerates due to an increased carrier–carrier scattering rate, while cooling slows down due to phonon bottleneck effects (Supplementary Figs. 5 and 6)[26–28,30].

We carried out fs-TAM measurements on film 1 photoexcited at 580 nm (2.14 eV) at an initial mean carrier density of 4.28×10^{17} cm^{-3}, a regime in which the hot phonon effect is negligible[30]. The high-energy side of the photobleaching band of the semiconductor is not only directly correlated with the electron and hole Fermi distribution, but also with the spectral features that stem from non-thermalized carriers[26]. As depicted in the schematic diagram of the energy dispersion relation in k space (Fig. 1c),
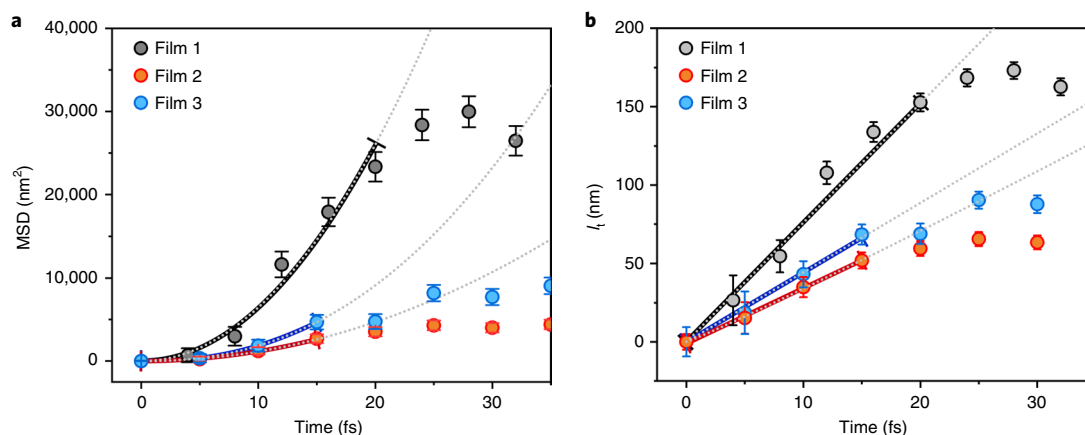
Fig. 2 | Spatial dynamics of non-equilibrium carriers. a, Time evolution of the MSD $= \sigma_t^2 - \sigma_0^2$ profile, where σ_0^2 is the width of the spatial carrier distribution obtained at zero pump–probe delay. The grey dotted lines represent fits using the power law equation, Dt^α. **b**, Time evolution of the relative changes in the ballistic transport length, $l_t = \sqrt{\sigma_t^2 - \sigma_0^2}$, in the ballistic transport region. The grey dotted lines represent the resultant fit of $l \approx \nu_t$, where ν is a coefficient that provides the velocity of ballistic transport. The colour lines represent the region of the best fit. Error bars represent the standard deviation widths from the 2D Gaussian fit as discussed in detail in Supplementary Section 4.

initially the generated carriers assume a non-equilibrium distribution around the pump energy[23]. Concomitant phase-space and band-filling effects lead to a strong photobleaching band and a broad high-energy tail[29]. The non-equilibrium carriers then undergo carrier–carrier scattering within tens of femtoseconds and their energy is redistributed to form a quasi-equilibrium carrier distribution, with enhanced and broad spectra near E_g. This population subsequently cools over hundreds of femtoseconds to reach a thermal equilibrium with the lattice. Consequently, by monitoring carriers generated around the pump energy or at the high-energy side of the photobleaching band, we can explore the spatial transport dynamics of non-equilibrium carriers.

Figure 1d shows the fs-TAM images obtained from film 1, probing at the high-energy tail of the photobleaching band (~720 nm), that is, the non-equilibrium carrier distribution. We note that the fs-TAM images of each film were obtained by averaging the images taken over 50 runs on at least five different spots across multiple films, to eliminate artefacts from spot-to-spot variations in the sample. The x–y axis in Fig. 1d plots the spatial position and the z axis (in false colour) gives the signal strength at each spatial position. Each image provides the spatial profile of the carrier distribution. Intriguingly, the fs-TAM images recorded as a function of time clearly reveal a pronounced spatial expansion of the carrier distribution within a few tens of femtoseconds. This implies that carriers are moving rapidly at the earliest times after photoexcitation.

To quantify the spatiotemporal evolution, we fitted the fs-TAM images with an isotropic two-dimensional (2D) Gaussian function (Supplementary Section 3) and extracted the corresponding σ, as shown in Fig. 1e (Supplementary Figs. 7–10)[17]. At zero-time delay the fs-TAM signal is expected to be spatially distributed only within the pump area. Consistent with this we found that the width of the fs-TAM signal obtained at a near-zero pump–probe delay, σ_0, was close to the diffraction limit of our microscope (166 ± 10 nm versus 139 nm for a diffraction-limited spot (Supplementary Fig. 11 and Supplementary Table 1), which represents the initial carrier distribution. Shortly after photoexcitation, a rapid expansion of the carrier distribution occurred, which we quantified by calculation of the mean-squared displacement (MSD $= \sigma_t^2 - \sigma_0^2$), as plotted in Fig. 2a (black). We found that the MSD of the non-equilibrium carriers in film 1 grew non-linearly, in contrast to the linear behaviour expected for normal diffusion. Furthermore, the MSD within the first 20 fs is well described by a power law fit, $\sigma_t^2 - \sigma_0^2 = Dt^\alpha$, giving an α value of

2.00 ± 0.30 (where D is the diffusion coefficient). $\alpha = 2$ signifies that the non-equilibrium carriers in film 1 propagate in a ballistic manner during the initial 20 fs after photoexcitation. In Fig. 2b, we plot the relative change in the width of the carrier distribution according to $l_t = \sqrt{\sigma_t^2 - \sigma_0^2}$ as a function of time. The linear region in this plot, shown via the fits, gives the ballistic carrier transport length. For film 1, this value is measured to be $l = 153 \pm 6$ nm, a remarkably large distance. No comparable ultrafast microscopy measurements have been performed for other semiconductor systems, but electrical measurements in GaAs transistors suggest a ballistic transport lengths of 85 nm (ref. [31]).

To investigate the effect of film morphology on the ballistic transport dynamics of the non-equilibrium carriers, we conducted fs-TAM measurements on films 2 and 3 (fabrication in Method). The scanning electron microscopy images for all the thin films exhibited polygon grains; films 1 and 3 exhibited large voids in the vicinity of grains, as shown in Fig. 3d,e and Supplementary Fig. 1. We emphasize that in all the films the grain size (about 2, 20 and 1 μm for films 1, 2 and 3, respectively) is at least twice as large as the pump spot size used in fs-TAM, which thus provides a quasi-single crystalline condition for our measurements (Supplementary Figs. 1 and 12). These grain sizes are also typical of perovskite films used in high-performance devices.

As shown in Fig. 2a (red and blue lines), similar to film 1, the MSD traces for films 2 and 3 are well described by a power law fit at very early times (up to 15 fs). The obtained α values of ~2 (2.04 ± 0.12 and 2.30 ± 0.04 for films 2 and 3, respectively) match those obtained for film 1 and provide strong evidence that the ballistic transport of non-equilibrium carriers is universal in MAPI$_{3-x}$Cl$_x$ thin films in spite of different film-fabrication protocols and morphology. However, despite having similar α values, the expansion obtained for films 2 and 3 is significantly reduced and stops slightly earlier at ~15 fs. As shown in Fig. 2b, the ballistic transport lengths of films 2 and 3 were determined to be 52 ± 5 and 68 ± 6 nm, respectively, much shorter than that of film 1. This suggests that all films support ballistic transport at early times, but the magnitude is controlled by the film morphology.

The ballistic transport of carriers in semiconductors is known to be sensitive to energetic disorder[32,33]. To assess the role of disorder, we performed steady-state PL microscopy measurements, which provide a sensitive probe of spatial disorder in the films. In Fig. 3a–c and Supplementary Fig. 13, we compare the wide-field PL intensity
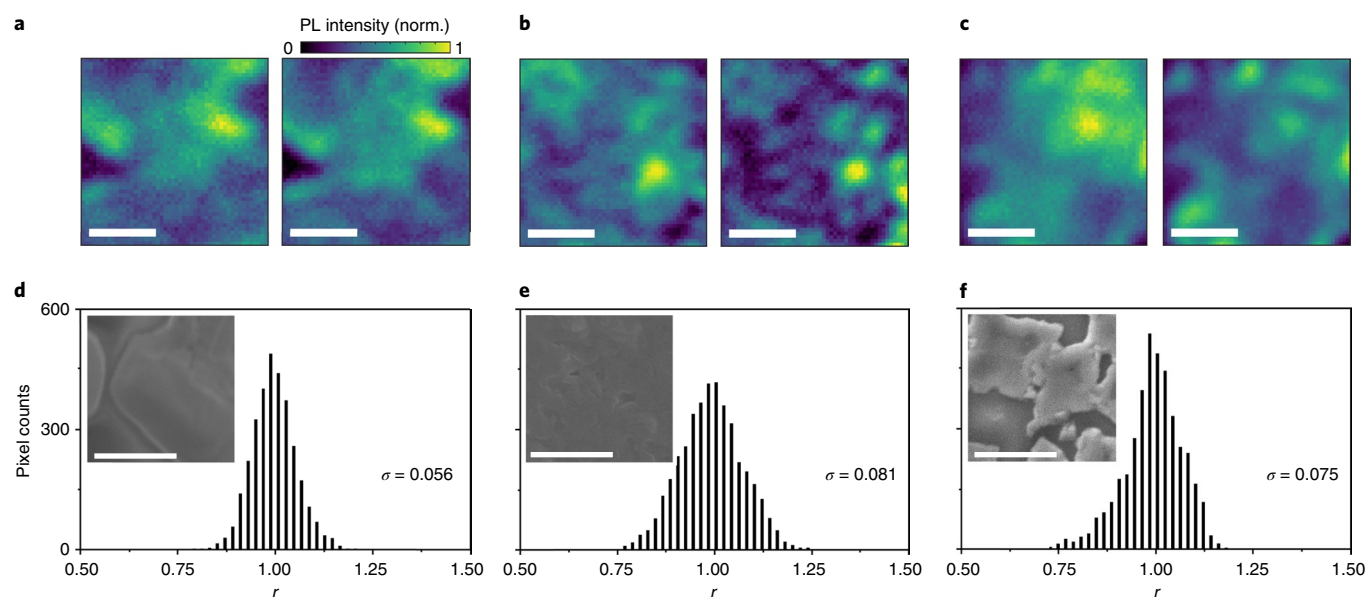
Fig. 3 | PL behaviour of three different perovskite thin films. a–c, The wide-field PL images recorded at 760 nm (1.63 eV) (left) and 790 nm (1.57 eV) (right) of films 1 (**a**), 2 (**b**) and 3 (**c**). Here we only plot representative images obtained at spot A (Supplementary Fig. 13) for each MAPI$_{3-x}$Cl$_x$ thin film. Additional PL images recorded at two additional spots (B and C) are shown in Supplementary Fig. 13. **d–f**, The histograms of the PL intensity ratio of films 1 (**d**), 2 (**e**) and 3 (**f**). To obtain the histograms, first, the PL intensity images were normalized (norm.) to 1, second, we calculated the PL intensity ratio between the two probe wavelengths by the equation $r_x = \frac{I_{x,760\,nm}+1}{I_{x,790\,nm}+1}$ and third, the histogram, which provides a visual representation of the PL intensity ratio distribution, was created. The σ values represent the width of each histogram and provide an estimate of the energetic disorder. Insets: representative scanning electron microscopy images for films 1, 2 and 3. Scale bars, 500 nm.

images of films 1, 2 and 3 recorded at 760 (left panels) and 790 nm (right panels). Any spatial energetic disorder in the films is reflected in its PL spectrum and hence leads to different spatial distributions of PL intensity between the two wavelengths. Whereas the PL intensity images of film 1 exhibit similar spatial distributions at 760 and 790 nm, films 2 and 3 exhibit different spatial distributions. This observation indicates that films 2 and 3 contain larger spatial energetic disorders than that of film 1. To quantify the underlying disorder, we computed the PL intensity ratio r_x, where x is the position within each film, and produced corresponding histograms from the spatial maps, as shown in Fig. 3d–f and Supplementary Fig. 13. The histograms of film 1 display a tight distribution with a σ of 0.056. By contrast, the histograms of films 2 and 3 exhibit a much broader distribution with σ values of 0.081 and 0.075, respectively. These measurements are indicative that the spatial energetic disorder in the films increases from film 1 to film 3 to film 2. As the ballistic transport length decreases in the same order (Supplementary Fig. 14), we propose that the energetic disorder limits the ballistic transport length of the non-equilibrium carriers in perovskite thin films.

To elucidate the effect of carrier density on the ballistic transport dynamics of the non-equilibrium carriers, we performed fs-TAM measurements as a function of pump fluence with an initial mean carrier density that ranged from 5.40×10^{17} to 2.50×10^{18} cm^{-3} (Supplementary Figs. 15–17). We compared film 1 (Fig. 4a), which showed the lowest energetic disorder and longest ballistic transport length, with film 2 (Fig. 4b), which exhibited the highest energetic disorder and shortest ballistic transport length. For film 1 we found that as the mean carrier density increased from 5.40×10^{17} to 2.50×10^{18} cm^{-3}, the corresponding ballistic transport length reduced from 153 ± 6 to 66 ± 10 nm (Fig. 4a,c). This suggests that in this sample at higher carrier densities, carrier–carrier scattering is the dominant process to limit ballistic transport. When disorder is sufficiently low the non-equilibrium carriers have more time to move ballistically and travel further before they scatter with other

carriers. As the carrier density increases, the motion of the non-equilibrium carriers becomes more confined, which leads to a reduced transport length. We note that at a high fluence there is a saturation behaviour of the differential transmission ($\Delta T/T$) signal, whereas at the lower fluences at which we measured the large ballistic transport lengths, the $\Delta T/T$ signal scales linearly with the pump fluence, which indicates the lack of non-linear effects on the expansion (Supplementary Section 6).

In sharp contrast, for film 2 there is no noticeable difference in the ballistic transport length (52 ± 11, 49 ± 11 and 49 ± 10 nm (Fig. 4b,c)) with changes in the carrier density. This suggest that in a highly energetically disordered film, such as film 2 (Fig. 3b), the ballistic transport breaks down before carriers have a chance to scatter off each other and it is the spatial energetic disorder that limits transport. We furthermore found for film 1 that the ballistic transport length for carrier densities below 1.28×10^{18} cm^{-3} exhibited almost identical values (Fig. 4c, grey curve) despite a difference in the initial carrier density of a factor of three. This observation indicates that below a certain carrier density threshold carrier–carrier scattering no longer governs the ballistic transport distance and instead energetic disorder takes over.

The mean carrier transport velocity of 5.0×10^6 m s^{-1} extracted from the time-evolution profiles of ballistic transport length (7.6×10^6, 4.4×10^6 and 2.9×10^6 m s^{-1} for films 1, 2 and 3, respectively, as shown in Fig. 2b) is in approximate agreement with the group velocity of electrons within the conduction band as modelled by density functional theory in conjunction with the HSE exchange-correlation functional (approaching 1.0×10^6 m s^{-1} (Supplementary Fig. 18; Supplementary Section 7 gives details of the calculations)). This implies that photogenerated carriers propagate at the group velocity (Fig. 1c) and have a non-interacting nature at least at the earliest times after photon absorption[29]. This also helps rationalize our observations on the relationship between energetic disorder and ballistic transport lengths, as the disordered regions would act
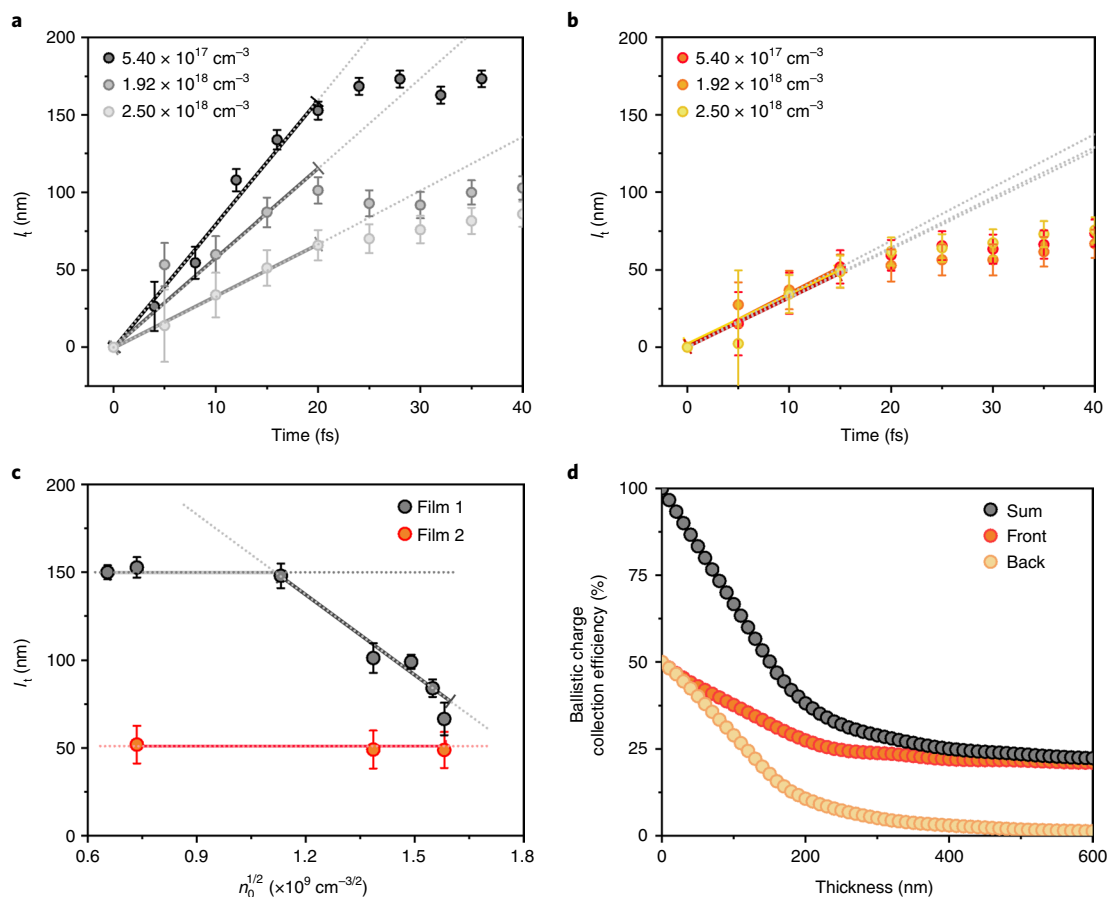
Fig. 4 | Ballistic transport of non-equilibrium carriers. a, Carrier-density dependence on the transport length, l_t, of film 1. **b**, Carrier-density dependence on the transport length of film 2. The spatial evolutions of both films 1 and 2 were obtained at 720 nm after excitation at 580 nm. The pump energy was varied between 150 and 900 fJ. **c**, The ballistic transport length plotted as a function of the square root of carrier density to take account of the bimolecular nature of carrier–carrier scattering. The ballistic transport distances were obtained at 20 and 15 fs for films 1 and 2, respectively, by using $l_t = \sqrt{\sigma_t^2 - \sigma_0^2}$. **d**, The ballistic charge collection efficiency, defined as the fraction of non-equilibrium carriers that reach the charge transport layers ballistically, plotted as a function of the thickness of the perovskite layer. The charge collection efficiency curves were obtained by assuming that the non-equilibrium carriers have a ballistic transport length of 150 nm. Error bars represent the standard deviation widths from the 2D Gaussian fit as discussed in detail in Supplementary Section 4.

as scattering sites whose effect is to halt the ballistic propagation. Future theoretical and experimental work is needed to identify the exact details of the disorder-induced scattering processes, but it is evident from the results presented here that energetic disorder plays a large role in the process and to reduce spatial energetic disorder is a clear route to increasing ballistic transport lengths.

We stress that our observation of ballistic transport relates only to non-equilibrium carriers, before scattering disrupts their propagation on a timescale of tens of femtoseconds. Once this ballistic propagation broke down, we observed no further rapid transport of quasi-equilibrium hot carriers up to 5 ps (Supplementary Fig. 8; Supplementary Sections 8 and 9 give the details). Consequently, hot carriers do not play a significant role in the operating mechanism of PV devices under normal conditions. In contrast, the non-equilibrium carriers studied here could play a role, as ballistic transport operates under low excitation densities relevant to working PV devices. The continuous nature of solar illumination (air mass (AM) 1.5G (global) condition) leads to carrier densities of 10^{14}–10^{15} cm^{-3} for perovskite PV devices due to their long carrier lifetime of several hundreds of nanoseconds, which results in a carrier density two orders of magnitude lower than those studied here and implies a significantly reduced carrier-carrier scattering[23]. Furthermore, unlike for pulsed excitation, solar illumination continuously produces carriers and a majority of carriers at any time are

part of the cold population, for which the scattering cross-section will be reduced. Thus, in a working device under solar illumination, carriers can move at the group velocity, that is, ballistically, immediately after photogeneration until scattered by other carriers or localized by disorder within the film. Based on the measurements here, carriers are able to propagate with a ballistic transport distance of at least 150 nm under operational device conditions.

To understand the possible effect of ballistic transport on the performance on a working perovskite device, we constructed a full optical model for a device using the transfer matrix formalism, taking into account electrodes, charge transport layers and an active layer of variable thickness (Supplementary Section 10 gives full details of the model). We used a ballistic transport distance of 150 nm, which is the value measured in film 1. Figure 4d plots the ballistic charge collection efficiency, that is, the fraction of carriers that reach the charge collection layers ballistically, as a function of the thickness of the perovskite film. Values are shown for collection at both the front and back charge transport layer and also for the sum. For very thin films a large fraction of the carriers can reach the charge collection layer ballistically, whereas for films of thickness 400–600 nm, which are typical for PV devices, 25% of the carriers can reach the charge collection layer ballistically. This value effectively saturates due to the absorption profile of light within the device, with a large fraction of light absorbed towards the front

of the device (Supplementary Section 10 gives details). Although transport to the charge collection layer is separate from charge injection in these layers, these results suggest that ballistic transport could play a significant part role in devices. It is possible that future charge collection and injection contacts could be engineered to harness these effects for a range of device applications.

Our results demonstrate that non-equilibrium carriers can propagate ballistically over distances of 150 nm in perovskite thin films. Such ballistic motion has, so far, not been considered to be of relevance in PV operation and our results call for a re-evaluation of the current device models. Moreover, future materials and devices can be engineered to efficiently harness the phenomena to create improved and novel functionalities. Our experimental methodology also shows that the long-standing challenges of simultaneously achieving a high temporal resolution and a high spatial localization precision are surmountable and pave the way towards the nanoscale-sensitive characterization of optically induced electronic processes on the femtosecond timescale.

Online content

References

1. Tan, Z. et al. Bright light-emitting diodes based on organometal halide perovskite. *Nat. Nanotechnol.* **9**, 687–692 (2014).
2. Burschka, J. et al. Sequential deposition as a route to high-performance perovskite-sensitized solar cells. *Nature* **499**, 316–319 (2013).
3. Senanayak, S. P. Understanding charge transport in lead iodide perovskite thin-film field-effect transistors. *Sci. Adv.* **3**, e1601935 (2017).
4. Lee, M. M., Teuscher, J., Miyasaka, T., Murakami, T. N. & Snaith, H. J. Efficient hybrid solar cells based on meso-superstructured organometal halide perovskites. *Science* **338**, 643–648 (2012).
5. Chin, X. Y., Cortecchia, D., Yin, J., Bruno, A. & Soci, C. Lead iodide perovskite light-emitting field-effect transistor. *Nat. Commun.* **6**, 1–9 (2015).
6. Xing, G. et al. Low-temperature solution-processed wavelength-tunable perovskites for lasing. *Nat. Mater.* **13**, 476–480 (2014).
7. Herz, L. M. Charge-carrier dynamics in organic–inorganic metal halide perovskites. *Annu. Rev. Phys. Chem.* **67**, 65–89 (2016).
8. Ulbricht, R., Hendry, E., Shan, J., Heinz, T. F. & Bonn, M. Carrier dynamics in semiconductors studied with time-resolved terahertz spectroscopy. *Rev. Mod. Phys.* **83**, 543–586 (2011).
9. Shah, J. *Ultrafast Spectroscopy of Semiconductors and Semiconductor Nanostructures* Ch. 7 (Springer, 2006).
10. Li, W. et al. Chemically diverse and multifunctional hybrid organic–inorganic perovskites. *Nat. Rev. Mater.* **2**, 1–18 (2017).
11. Brenner, T. M., Egger, D. A., Kronik, L., Hodes, G. & Cahen, D. Hybrid organic–inorganic perovskites: low-cost semiconductors with intriguing charge-transport properties. *Nat. Rev. Mater.* **1**, 1–16 (2016).
12. Huang, J., Yuan, Y., Shao, Y. & Yan, Y. Understanding the physical properties of hybrid perovskites for photovoltaic applications. *Nat. Rev. Mater.* **2**, 1–19 (2017).
13. García De Arquer, F. P., Armin, A., Meredith, P. & Sargent, E. H. Solution-processed semiconductors for next-generation photodetectors. *Nat. Rev. Mater.* **2**, 1–15 (2017).
14. Stranks, S. D. et al. Electron-hole diffusion lengths exceeding 1 micrometer in an organometal trihalide perovskite absorber. *Science* **342**, 341–344 (2013).
15. Xing, G. et al. Long-range balanced electron- and hole-transport lengths in organic–inorganic $CH_3NH_3PbI_3$. *Science* **342**, 344–347 (2013).
16. Guo, Z. et al. Long-range hot-carrier transport in hybrid perovskites visualized by ultrafast microscopy. *Science* **62**, 59–62 (2017).
17. Guo, Z., Manser, J. S., Wan, Y., Kamat, P. V. & Huang, L. Spatial and temporal imaging of long-range charge transport in perovskite thin films by ultrafast microscopy. *Nat. Commun.* **6**, 7471 (2015).
18. Brédas, J. L., Sargent, E. H. & Scholes, G. D. Photovoltaic concepts inspired by coherence effects in photosynthetic systems. *Nat. Mater.* **16**, 35–44 (2016).
19. Von Diezmann, A., Shechtman, Y. & Moerner, W. E. Three-dimensional localization of single molecules for super-resolution imaging and single-particle tracking. *Chem. Rev.* **117**, 7244–7275 (2017).
20. Schnedermann, C. Ultrafast tracking of exciton and charge carrier transport in optoelectronic materials on the nanometer scale. *J. Phys. Chem. Lett.* **10**, 6727–6733 (2019).
21. Nah, S. et al. Ultrafast imaging of carrier cooling in metal halide perovskite thin films. *Nano Lett.* **18**, 1044–1048 (2018).
22. Schnedermann, C. et al. Sub-10 fs time-resolved vibronic optical microscopy. *J. Phys. Chem. Lett.* **7**, 4854–4859 (2016).
23. Richter, J. M. et al. Ultrafast carrier thermalization in lead iodide perovskite probed with two-dimensional electronic spectroscopy. *Nat. Commun.* **8**, 1–7 (2017).
24. Jha, A. et al. Direct observation of ultrafast exciton dissociation in lead iodide perovskite by 2D electronic spectroscopy. *ACS Photon.* **5**, 852–860 (2018).
25. Zhao, B. et al. High open-circuit voltages in tin-rich low-bandgap perovskite-based planar heterojunction photovoltaics. *Adv. Mater.* **29**, 1604744 (2017).
26. Price, M. B. et al. Hot-carrier cooling and photoinduced refractive index changes in organic–inorganic lead halide perovskites. *Nat. Commun.* **6**, 8420 (2015).
27. Manser, J. S. & Kamat, P. V. Band filling with free charge carriers in organometal halide perovskites. *Nat. Photon.* **8**, 737–743 (2014).
28. Yang, Y. et al. Observation of a hot-phonon bottleneck in lead-iodide perovskites. *Nat. Photon.* **10**, 53–59 (2016).
29. Hunsche, S., Leo, K., Kurz, H. & Kohler, K. Exciton absorption saturation by phase-space filling: influence of carrier temperature and density. *Phys. Rev. B* **49**, 16565–16568 (1994).
30. Fu, J. et al. Hot carrier cooling mechanisms in halide perovskites. *Nat. Commun.* **8**, 1–9 (2017).
31. Hayes, R. & Levi, A. Dynamics of extreme nonequilibrium electron transport in GaAs. *IEEE J. Quantum Electron.* **22**, 1744–1752 (1986).
32. Beenakker, C. W. J. & van Houten, H. Quantum transport in semiconductor nanostructures. *Solid State Phys.* **44**, 1–228 (1991).
33. Zhang, W. et al. Enhanced optoelectronic quality of perovskite thin films with hypophosphorous acid for planar heterojunction solar cells. *Nat. Commun.* **6**, 1–9 (2015).

Methods

Sample preparation. All the materials were purchased from Sigma-Aldrich or Dysol and were used as received. A mixture of $PbCl_2$ and CH_3NH_3I in a 1:3 molar stoichiometric ratio was prepared in N,N-dimethylformamide solvent by constant stirring until it dissolved. Film 1 was prepared by using the cold-casting method, in which the solution was spin coated on top of clean glass substrates at 2,000 r.p.m. for 60 s and annealed at 100 °C for 5 min to form thin films. Film 2 was prepared by the hot-casting method. A hot (~70 °C) solution was cast onto a substrate maintained at a temperature of up to 180 °C and subsequently spin coated (15 s). Finally, it was annealed at 100 °C to obtain a uniform film. Both films 1 and 2 were fabricated and encapsulated inside a nitrogen-filled glove box. However, film 3 was fabricated under an air atmosphere by using the cold-casting method as described above.

Femtosecond transient absorption spectroscopy. The ultrafast (15 fs time resolution) transient absorption experiments were performed using a Yb:KGW (potassium gadolinium tungstate)-based amplified system (Pharos, Light Conversion) to provide 14.5 W at 1,030 nm with a 38 kHz repetition rate. The probe beam was generated by focusing a portion of the fundamental in a 4 mm yttrium aluminium garnet (YAG) crystal to generate a white light continuum (WLC). The pump beam was generated using a non-collinear optical parametric amplifier (NOPA). The WLC generated from the 3 mm YAG crystal was focused onto the non-linear crystal (37° cut barium borate, type I, 5° external angle) and were pumped by the third harmonic of the fundamental (HIRO, Light Conversion). The NOPA output consisted of 600 μW pump pulses at a centre wavelength of 525 nm and spectral bandwidth of 25 nm. The pump pulses were then compressed using a pair of chirped mirrors. The 525 nm NOPA pump pulses and WLC probe beam overlapped in the sample with a 8.7° angle. The WLC probe beam was delayed using a computer-controlled piezoelectric translation stage. A sequence of probe pulses with and without a pump was generated using a chopper wheel on the pump beam. After the sample, the probe pulses were seeded through a monochromator and a silicon line scan camera (AVIIVA EM2/EM4) used to measure the transient difference absorption between 540 and 1,000 nm at a 19 kHz rate.

fs-TAM. A Yb:KGW laser system (Pharos, Light Conversion) provided 200 fs, 30 μJ pulses at 1,030 nm with 200 kHz repetition rate. The output beam was divided by a beam splitter and seeded two broadband WLC stages. The probe WLC was generated in a 3 mm YAG crystal and adjusted to cover the wavelength range from 650 to 950 nm by a fused-silica prism-based spectral filter. In contrast, the pump WLC was generated in a 3 mm sapphire crystal to extend the WLC to 500 nm, and short-pass filtered at 650 nm (FESH650, Thorlabs). A set of chirped mirrors (pump, 109811, Layertec; probe, DCM9, Venteon) and a pair of fused silica wedges (Layertec) compressed the pulses to 9.2 fs (pump) and 6.8 fs (probe), as verified by second-harmonic generation frequency-resolved optical gating (Supplementary Section 2). In addition, the pump pulse was precompressed with another set of chirped mirrors (109811, Layertec) to account for dispersion in the microscope optics. The corresponding cross-correlation curve simulated with the retrieved pump and probe temporal profiles given in Supplementary Section 2 shows an effective time resolution of 13 fs. A closed-looped piezo translation stage (P-625.1CL, Physik Instrumente) was used to delay the probe with respect to the pump. A clean TEM00 mode for the pump was achieved with a pinhole. The pump was collimated to completely fill the aperture of the objective lens and was focused onto the sample by an oil immersion objective (×100, an effective numerical aperture, NA, of 1.1) to the near diffraction-limited spot (~270 nm (FWHM)) as the probe pulse was delivered into the sample with a relatively large focal spot (~15 μm) from the opposite direction. The transmitted probe pulse was collected by the same objective and sent to an EMCCD camera (Rolera Thunder, QImaging). The total magnification of the imaging system was ×288. The scattered pump light was rejected by a 650 nm long-pass filter (FEL650, Thorlabs) inserted in front of the camera. Differential imaging was achieved by modulating the pump beam at 30 Hz by a mechanical chopper. Moreover, fs-TAM images were obtained by averaging images taken over 50 runs at 10 different spots for low pump fluence measurements and at 5 different spots for relatively high fluence measurements for each sample.

Data availability

The data underlying all figures in the main text and supplementary information are publicly available at https://doi.org/10.17863/CAM.44851.

Author contributions

C.S., J.S., J.M.L. and P.K. designed the TAM experiments. J.S. carried out TAM measurements with L.P. J.S. and A.R. analysed the data and wrote the paper. L.N. and A.S. fabricated the MAPI thin films. H.-K.K. performed the scanning electron microscopy measurements. R.Y.S.C. and C.C. simulated the charge collection model. B.M. performed the computational simulations. P.K. and A.R. supervised the work.

Competing interests

The authors declare no competing interests.

Additional information

Supplementary information is available for this paper at https://doi.org/10.1038/s41567-019-0730-2.

Correspondence and requests for materials should be addressed to P.K. or A.R.

Reprints and permissions information is available at www.nature.com/reprints.